Moving Target Refocusing With the FMCW SAR System MIRANDA-35

Emiliano Casalini ⓘ, *Member, IEEE*, Julian Fagir ⓘ, *Member, IEEE*, and Daniel Henke ⓘ

Abstract—Inverse synthetic aperture radar is a commonly adopted technique for producing high-resolution images of moving targets. This article investigates the imaging capabilities of high-frequency and high-bandwidth systems by means of two distinct experiments. The deployed sensor is the Fraunhofer FHR MIRANDA-35, a millimeter-wave synthetic aperture radar airborne system, which transmits frequency-modulated continuous-wave signals at the Ka-band and is capable of achieving centimeter resolution. The performances are assessed by comparing the derived estimates (e.g., radial velocity and acceleration, and dimensions) with independent ground measurements. The resulting accuracy can be summarized as follows: the mean value of the percent error is 2.05% and 2.11% for radial velocity and acceleration, respectively, and 4.27% for the target dimensions.

Index Terms—Frequency-modulated continuous-wave (FMCW), inverse synthetic aperture radar (ISAR), MIRANDA-35, motion compensation (MoComp), radar imaging, synthetic aperture radar (SAR).

I. INTRODUCTION

SYNTHETIC aperture radar (SAR) systems are frequently exploited solutions for earth surface monitoring in all-weather and all-light conditions. Such systems are capable of producing electromagnetic images with enhanced spatial resolution [1] and, therefore, are a useful tool for, among many applications, surveillance and reconnaissance purposes [2], [3]. The need for a broad accessibility to SAR has led to the design of frequency-modulated continuous-wave (FMCW) waveforms [4]. FMCW SAR differentiates from pulsed SAR due to the transmission of a frequency-modulated signal, which covers most of the pulse repetition interval (PRI). As a consequence, high signal-to-noise ratio values can be obtained even when using low transmission powers, thus making the system more compact and cost-effective. A detailed analysis of the FMCW SAR signal model, its resulting signal processing aspects, and viable hardware solutions can be found in [5].

Conventional SAR processing is designed to compensate for the quadratic and higher-order phase terms produced by the static scene. As a consequence, moving target signals are not coherently integrated, thereby producing signatures that are both blurred and displaced along-track [6]. Many publications have dealt with the imaging of moving targets in SAR images [7]–[11]. In [7], Jao derives the moving target image impulse response and its spectrum, which is then used to perform matched filtering. A 2-D matched filtering without *a priori* knowledge of the accurate motion parameters can successfully correct the range cell migration [8]. Alternatively, well-known SAR processors can be adjusted for radar imaging purposes: a bank of focusing filters based on the chirp scaling algorithm can efficiently image moving targets [9]. Furthermore, the concept of normalized relative speed has been used to modify the wavenumber domain algorithm (WDA) for both pulsed [10] and FMCW SAR [11]. Though yielding fairly good results, the aforementioned algorithms are based upon simplified range history models, which are unlikely to hold, for instance, in maritime scenarios, where targets undergo complicated angular motions (e.g., roll, pitch, and yaw). This calls for more sophisticated techniques, such as inverse synthetic aperture radar (ISAR) [12], [13], which is capable of dealing with a wider range of target dynamics. Its main drawback is represented by the unpredictable azimuth resolution, which depends on the unknown target dynamics and cannot, therefore, be estimated beforehand. However, ISAR succeeds where most of algorithms fail, thus making it a powerful tool for a number of applications. In light of recent technological developments, ISAR theory has been generalized to include FMCW waveforms: in [14], Giusti and Martorella analyze the image distortions introduced when using such signals and present a more general solution. However, FMCW ISAR algorithms, such as the one introduced in [14], were only applied to X-band datasets with meter scale range resolution. It remains an open question as to whether such algorithms can successfully process datasets acquired at higher frequencies and with larger bandwidths.

In this article, we introduce the Ka-band Fraunhofer FHR MIRANDA-35 experimental sensor [15]. Its radar imaging capabilities are discussed on the basis of experimental results obtained when combining state-of-the-art techniques, in a similar fashion to [16]. However, unlike previously published works, the implemented method comprises both pulsed and FMCW SAR techniques that have been developed separately and have never been used in combination. Moreover, in light of its main features (e.g., millimeter-wave wavelength, FMCW technology, and ultra-light-weight airborne platform), MIRANDA-35 results to be an interesting case study as the need for extremely compact and low-cost systems, yet characterized by satisfying

The authors are with Remote Sensing Laboratories, Department of Geography, University of Zürich, CH-8057 Zürich, Switzerland (e-mail: emiliano.casalini@geo.uzh.ch; julian.fagir@geo.uzh.ch; daniel.henke@geo.uzh.ch).
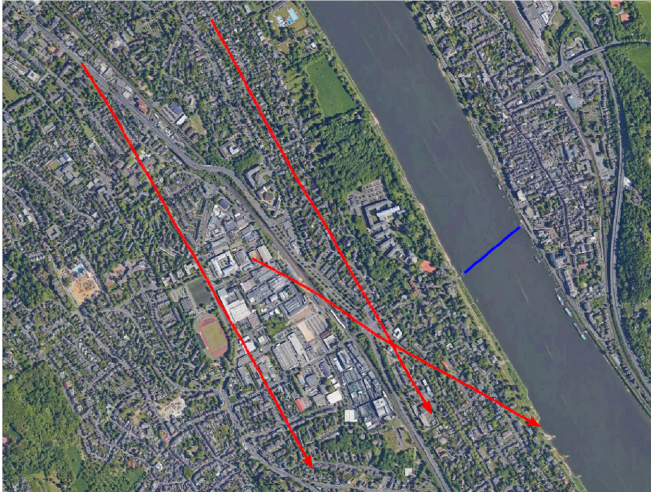
Fig. 1.   Experiment 1. Google Earth image of the *Königswinter* test-site: sensor's flightpaths (red) and target's path (blue).

TABLE I
SYSTEM AND MOTION PARAMETERS: EXPERIMENT 1

Data-take	#1	#2	#3
Bandwidth [GHz]	0.6	1.25	0.6
PRF [kHz]	10.17	2.54	10.17
Mid-range [m]	622.39	1247.20	622.39
Swath width [m]	235.5	455.47	235.5
Velocity [$\mathrm{m\,s^{-1}}$]	32.63 ± 0.09	35.33 ± 0.03	30.84 ± 0.04
Roll [deg]	0.79 ± 1.23	2.25 ± 0.49	2.33 ± 0.84
Pitch [deg]	-1.35 ± 0.07	-0.17 ± 0.06	1.71 ± 0.23
Yaw [deg]	156.15 ± 0.11	159.56 ± 0.52	126.74 ± 0.14

TABLE II
SYSTEM AND MOTION PARAMETERS: EXPERIMENT 2

Data-take	#1	#2	#3
Bandwidth [GHz]	1	1	1
PRF [kHz]	1.69	1.27	1.69
Mid-range [m]	2003.32	2916.46	2003.32
Swath width [m]	791.06	1078.78	791.06
Velocity [$\mathrm{m\,s^{-1}}$]	54.09 ± 0.07	54.18 ± 0.04	55.17 ± 0.02
Roll [deg]	-0.18 ± 0.23	-0.13 ± 0.19	-0.46 ± 0.10
Pitch [deg]	0.34 ± 0.04	0.22 ± 0.13	-0.74 ± 0.02
Yaw [deg]	103.37 ± 0.24	105.48 ± 0.05	100.78 ± 0.11

performances, is raising. Finally, the results presented herein are of importance as FMCW ISAR processing has never been tested with Ka-band datasets. At such wavelengths, the target range history needs to be estimated with millimeter accuracy, thereby making the refocusing task way more challenging.

The remainder of this article is organized as follows. In Section II-A, we introduce the MIRANDA-35 sensor and its specifications and describe the experiments' setups. Section II-B reviews the implemented processing chain, whereas Section II-C describes the available ground measurements used for validation. The obtained performances were assessed by processing real datasets acquired during two different experiments, and they are summarized in Sections III-A and III-B. Results and future research directions are thoroughly discussed in Section IV.

II. METHOD

A. Sensor and Experimental Setup

The SAR sensor utilized in the experiments was the Fraunhofer FHR MIRANDA-35 system [15]. This is an airborne sensor transmitting FMCW signals and operating at 35 GHz frequency. The system is composed of one transmitting and up to four receiving antennas, which can be arranged both along- and cross-track, thereby allowing for a variety of applications. The minimum and maximum pulse repetition frequency (PRF) is 1271.57 and 10172.53 Hz, respectively, whereas the largest usable bandwidth is equal to 1.25 GHz, thus defining a maximum range resolution of 12 cm. Due to its compactness, MIRANDA-35 is mounted on board the ultra-light-weight FHR Delphin platform. Two experiments, held during distinct campaigns, are briefly discussed here.

1) Experiment 1: The experiment was conducted in Summer 2018 in the municipality of *Königswinter*, in the district *Rhein-Sieg*, Germany. The mission was designed in order to record the activities of the ferry *Königswinter IV*. The experimental setup is depicted in Fig. 1. The nominal values of the most notable system parameters, together with mean and standard deviation of the platform motion parameters, are listed in Table I.

2) Experiment 2: The experiment was conducted in Summer 2017 in the surroundings of the town of *Thun*, in the canton of *Bern*, Switzerland. The mission was designed in order to study the case of a ground target (i.e., a medium-sized truck) moving at moderate speed along a linear trajectory. The target of interest was equipped with four dihedral corner reflectors attached on two poles at different heights. Table II summarizes the nominal values of the main system parameters, and additionally, it provides mean and standard deviation of the platform motion parameters. For a more detailed description of the experiment, see [11].

B. Processing Chain

The main steps of the implemented algorithm are summarized in the block diagram of Fig. 2, where intermediate Fourier transforms (FTs) and other minor operations are omitted for the sake of clarity. The input consists of a processed SAR image in radar geometry (i.e., range and cross-range), whereas the output consists of the target refocused signature. The implemented algorithm is capable of dealing with images produced by any focusing algorithm as long as the proper image inversion mapping is exploited. The examples shown within this article, and thus the related inversion mapping, were produced on the basis of the WDA for FMCW signals [17].
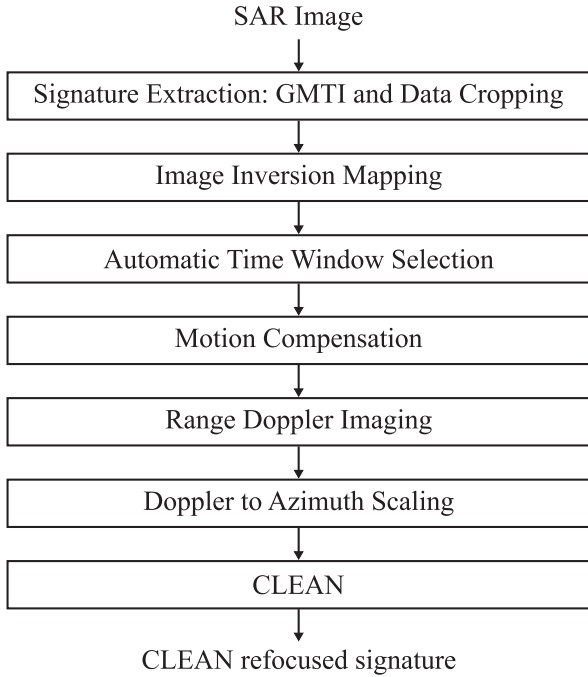
SAR Image
↓

Signature Extraction: GMTI and Data Cropping
↓

Image Inversion Mapping
↓

Automatic Time Window Selection
↓

Motion Compensation
↓

Range Doppler Imaging
↓

Doppler to Azimuth Scaling
↓

CLEAN
↓

CLEAN refocused signature

Fig. 2. Block diagram of the implemented algorithm.

1) GMTI and Data Cropping: The multiple spatial degrees of freedom offered by MIRANDA-35 are exploited in order to perform along-track interferometry [18]. The resulting interferogram is passed on to a 2-D adaptive nonparametric constant false alarm rate detector to determine whether the pixel of interest is occupied by a moving target [19]. This technique estimates the magnitude-phase joint probability density function of the terrain interferogram via a histogram-based approach, and it detects potential moving targets by exploiting a threshold contour line. Then, the derived detections are grouped together and denoised by means of morphological filtering [20]. Consequently, contiguous objects generated by the same target are connected by making use of the border tracing algorithm presented in [21]. Finally, a rectangular crop is defined based on centroid and size of the final object, and the useful signal is extracted from the SAR image.

2) Image Inversion Mapping: The image inversion mapping is designed on the basis of the focusing technique that was used to produce the algorithm input. The examples shown within this article were obtained by making use of the WDA for FMCW signals [17]: such an algorithm has proven itself capable of handling high-squint configurations, thereby making it suitable for an ultra-light-weight airborne platform. Its main steps are listed sequentially in the order they are performed: residual video phase (RVP) removal, reference function multiplication (RFM), and Stolt interpolation. The latter represents the main core of the WDA: it is implemented in the 2-D wavenumber domain and is designed to linearize the phase content of the data.

The obtained crop, which is represented in radar geometry, can be remapped in the 2-D wavenumber domain by performing an inverse Fourier transform (IFT) and an FT along the range and azimuth axis, respectively. Let the azimuth wavenumber be

referred to as k_x, whereas the slant-range and range wavenumber (i.e., the variable describing the signal along the range direction before and after applying the Stolt interpolation) are k_w and k_r, respectively. The inversion mapping can be formulated as

$$k_r \rightarrow k_w \tag{1}$$

where the relation between the different wavenumbers is as follows:

$$k_r = \sqrt{(\alpha k_w)^2 - \left[\frac{v_p}{c}(\alpha k_w) + k_x\right]^2} \tag{2}$$

with v_p and c being the platform velocity and the speed of light, respectively, and α is the stationary case Doppler factor defined as

$$\alpha = \frac{1}{1 - \frac{v_p^2}{c^2}}. \tag{3}$$

The subsequent step consists of reintroducing the range-invariant phase contribution originally removed by the RFM. This is performed by multiplying the output of the inverse Stolt interpolation with a filter, whose phase response is expressed as

$$\Phi_{\mathrm{RFM}}(k_x, k_w; v_p)$$
$$= -\sqrt{(\alpha k_w)^2 - \left[\frac{v_p}{c}(\alpha k_w) + k_x\right]^2}\, r_{ref} + k_x(v_p t_s) \tag{4}$$

with t_s being the fast time. The last term in (4), i.e., $k_x(v_p t_s)$, is the range-invariant range walk, which is caused by the motion of the platform during transmission [5]. Finally, after mapping the signal into the range domain through an FT, the RVP term is restored by means of a filter, which introduces a range-dependent delay [4]. Its phase response can be expressed as follows:

$$\Phi_{\mathrm{RVP}}(r) = \frac{\pi}{\gamma}\left(\gamma\frac{2r}{c}\right)^2 \tag{5}$$

where γ and r represent the transmitted signal chirp rate and the range axis, respectively.

The term $(v_p/c)(\alpha k_w)$ in (2) and (4) is unique to FMCW SAR environments and describes the range-azimuth coupling produced by the sensor motion during the transmission of the signal. The pulsed SAR solution can be obtained by forcing the sensor position to be stationary during transmission, which is known as *stop-and-go* approximation. This can be factored into (1)–(5) by replacing $v_p = 0$.

3) Automatic Time Window Selection: The illumination time for a given target on ground varies greatly depending on a variety of factors (e.g., acquisition geometry, antenna pattern, relative motion between sensor and target, etc.). Within this time span, which can reach up to few seconds for airborne scenarios, the target motion results to be fairly complicated, and conventional imaging algorithms, such as the range–Doppler technique, fail. In order to successfully perform radar imaging, only a subset of the available echoes (i.e., a window) needs to be processed. Its selection is based on the maximum contrast automatic time window selection algorithm proposed in [22]: the image with the highest contrast determines the *optimum* window position and length.

4) Motion Compensation: Motion Compensation (Mo-Comp) is a crucial step for ISAR processing. The received signal exhibits a phase modulation, which is a function of the range variation over time between the focusing point and the antenna phase center. In case this contribution was not perfectly compensated for, the residual phase term would induce defocusing, thereby jeopardizing the successful interpretation of the final products. In [14], Giusti and Martorella designed a MoComp algorithm for FMCW SAR: as the *stop-and-go* approximation is no longer valid, the phase modulation results to be dependent on both the fast time t_s and the slow time variable n.

The received signal, which was derived in [14], can be expressed as follows:

$$S_b(t_s, n) = K'w(t_s, n, T_s)e^{j\phi_0(t_s,n)}$$

$$\times \int_V g(\boldsymbol{x})e^{j\phi(t_s,n,\boldsymbol{x})}d\boldsymbol{x} \qquad (6)$$

where $\boldsymbol{x}$ represents the position of a given scatterer, and $g(\cdot)$ is the target reflectivity function. The signal domain, which is identified by $w(\cdot)$, can be approximated as

$$w(t_s, n, T_s) \approx \text{rect}\left(\frac{t_s - nT_s}{T_s}\right) \qquad (7)$$

with T_s being the PRI. Furthermore, the exponential $\phi_0(\cdot)$ in (6) can be expressed as follows:

$$\phi_0(t_s, n) = -2\pi(f_c + \gamma t_s)\tau_0(t_s, n) + \pi\gamma\tau_0^2(t_s, n)$$

$$= -2\pi(f_c + \gamma t_s)\frac{2R_0(t_s, n)}{c}$$

$$+ \pi\gamma\left(\frac{2R_0(t_s, n)}{c}\right)^2 \qquad (8)$$

where f_c represents the transmitted signal carrier frequency and $R_0(t_s, n)$ describes the range history of the target focusing point.

In case no *a priori* knowledge was available, $R_0(t_s, n)$ would need to be estimated on the basis of the received signal, thereby introducing the concept of ISAR autofocusing. Autofocusing techniques can be subdivided into two different categories: parametric and nonparametric [23]. The examples shown within this article were obtained by exploiting the so-called image-contrast-based technique [24]. This is a parametric technique that models $R_0(t_s, n)$ via a finite-order polynomial as

$$R_0(t_s, n) = \sum_{n=0}^{N} \frac{a_n(t_s + nT_s)}{n!}. \qquad (9)$$

The polynomial degree N is empirically designed: for common maritime and ground targets, two coefficients (i.e., the radial velocity and acceleration) describe the range history with sufficient accuracy. On the other hand, the estimate of the polynomial coefficient a_n is obtained by maximizing the contrast of the refocused signature, and the optimization problem is solved by making use of the Nelder–Mead method.

Equation (9) emphasizes how the complexity of the MoComp crucially increases in FMCW SAR scenarios. In fact, the number of radial distances that needs to be estimated is equal to $N_f \times N_s$, with N_f and N_s being the number of estimates along the fast and slow time, respectively.

5) Range–Doppler Imaging: An FT performed along the slow time successfully implements the range–Doppler technique, provided that the Fourier domain of the received signal can be approximated with a rectangular grid. This is obtained when the following conditions are satisfied.

1) The effective rotation vector is approximately constant.
2) The variation of the viewing angle within the integration time is small.
3) The signal is narrowband [12], [13].

After implementation of the range–Doppler technique, the energy due to a given scatterer is concentrated at a specific Doppler frequency. Though the imaging formation process is fairly simple, the resulting output is represented in a nonhomogeneous range/Doppler domain, thus making it impossible to retrieve the desired geometric features.

6) Doppler to Cross-Range Scaling: Converting Doppler into cross-ranges is a mandatory step in order to represent the refocused signature in a homogeneous domain. As pointed out in [25], the slow-time signal produced by a given scatterer is dependent on the target dynamics. More precisely, both Doppler and chirp rate are a function of, among other parameters, the effective rotation vector modulus Ω_{eff}, which defines the total variation of the viewing angle within the integration time. The relation between the chirp rate and Ω_{eff} can be expressed as follows:

$$m_k = \frac{2f_0\Omega_{\text{eff}}^2}{c}r_k. \qquad (10)$$

Equation (10) describes a line with axes m_k and r_k representing the chirp rate and range of the kth scatterer, respectively. The points of such line can be obtained by making use of basic image and signal processing techniques. The point spread function (PSF) of a given scatterer is extracted through image segmentation and backprojected into the slow-time domain via an IFT. Consequently, the local polynomial FT is exploited in order to assess what chirp rate guarantees the best focusing. Then, provided that a meaningful set of scatterers is available, it is possible to estimate the slope of the line by means of a least square error approach, and thus to derive Ω_{eff}. Finally, Doppler frequencies can be converted into cross-ranges by making use of

$$\nu_k = -\frac{2f_0\Omega_{\text{eff}}}{c}c_k \qquad (11)$$

with ν_k and c_k being the Doppler frequency and cross-range of the kth scatterer, respectively.

7) Clean: The dominant scatterers of the refocused signature are extracted by making use of the CLEAN technique [26]. After estimation of the PSF of the ISAR system, position and complex amplitude of each scatterer are retrieved, and their contribution is iteratively removed from the image.

C. Validation Methods

Diverse ground measurements were collected during both experiments in order to validate the derived products. Pictures
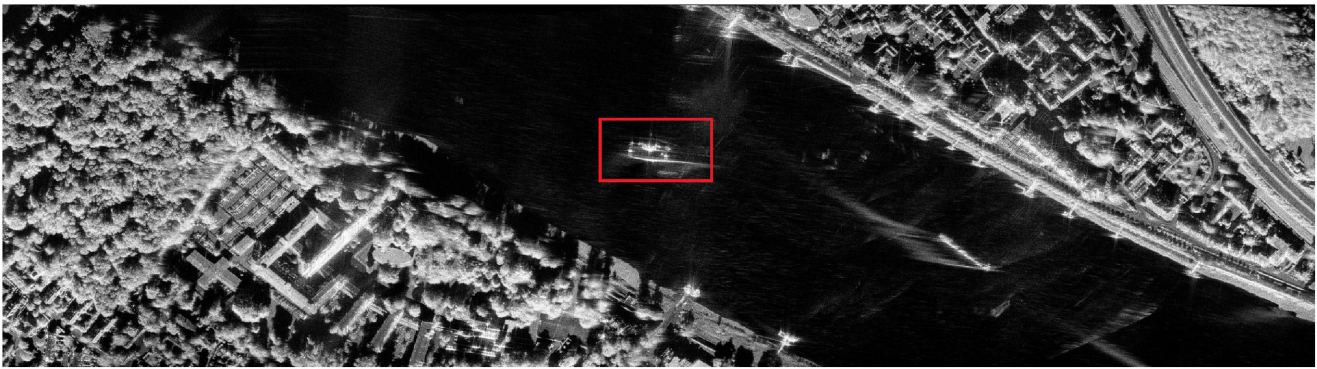
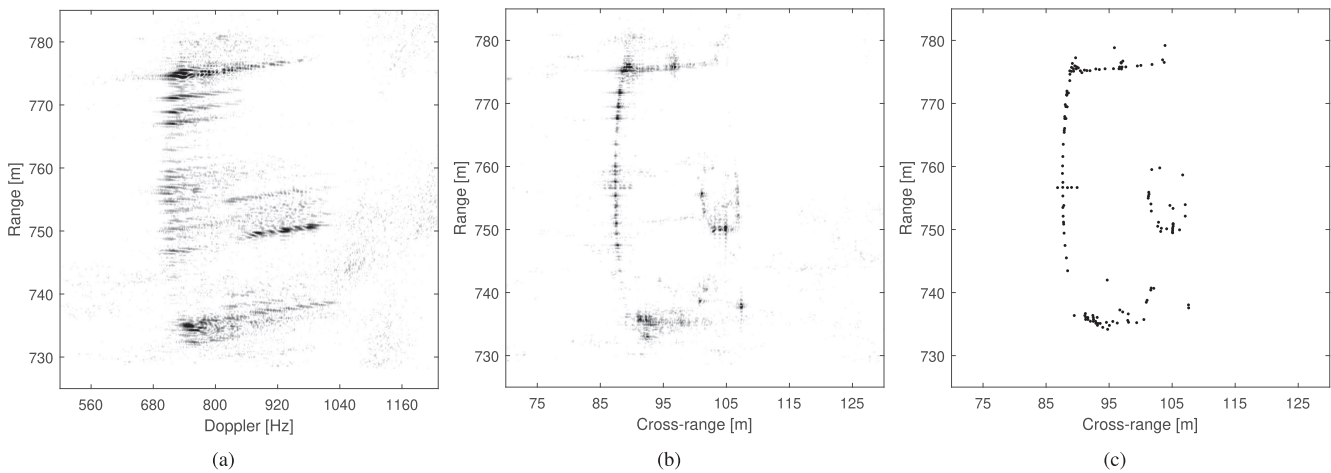Fig. 3. Experiment 1, exemplary SAR image: target of interest (red).

Fig. 4. Experiment 1, exemplary data-take. (a) Range/Doppler image before refocusing. (b) Range/cross-range image after refocusing. (c) CLEAN image.

of the illuminated area were taken by an optical camera installed on board the platform with a 2s sample interval. Moreover, both targets were equipped with differential GPS systems composed of a Trimble Zephyr 2 antenna and a Trimble R7 GNSS receiver. The estimated standard deviations of the GPS positions showed an approximately constant trend during the integration times, with values ranging between 0.026 and 0.040 m according to the specific data-take and experiment. The recorded dynamics are used in order to obtain the *true* radial velocity and acceleration, therefore allowing for an accurate validation of the motion estimates. Furthermore, for Experiment 1, the derived main geometric features (e.g., length and width) are compared with the design values obtained from the ferry's construction project.

III. RESULTS

A. Experiment 1

The exemplary SAR image depicted in Fig. 3 was fed to the implemented algorithm. The range/Doppler image of the target before refocusing is depicted in Fig. 4(a). The autofocusing algorithm converges when using $(v_r, a_r) = (-3.32\,\mathrm{m}\cdot\mathrm{s}^{-1}, 1.64\,\mathrm{m}\cdot\mathrm{s}^{-2})$, there by yielding the refocused image of Fig. 4(b). The estimated motion parameters were then compared with the ones provided by the GPSs, thus defining a percent error of

TABLE III
RESULTS: EXPERIMENT 1

Data-take	#1	#2	#3
(v_r, ϵ_{v_r})	$(-3.32, 1.78)$	$(-5.02, 2.67)$	$(-4.97, 2.65)$
(a_r, ϵ_{a_r})	$(1.64, 0.73)$	$(0.96, 5.05)$	$(1.31, 0.28)$
(L, ϵ_l)	$(44.55, 3.65)$	$(44.53, 3.70)$	$(43.03, 6.94)$
(W, ϵ_w)	$(19.36, 3.63)$	$(19.18, 4.53)$	$(19.46, 3.14)$

$^*[v_r] = \mathrm{m}\cdot\mathrm{s}^{-1}, [a_r] = \mathrm{m}\cdot\mathrm{s}^{-2}, [L] = \mathrm{m}, [W] = \mathrm{m}, [\epsilon] = \%.$

$(1.78\%, 0.73\%)$. Finally, the dominant scatterers of Fig. 4(b) were extracted by making use of the CLEAN technique and were exploited to derive the target length L and width W. The SAR derived dimensions are $(44.55\,\mathrm{m}, 19.36\,\mathrm{m})$, thus defining a percent error of $(3.65\%, 3.63\%)$. The remaining data-takes were processed through the same procedure: the refocused images, superimposed with the extracted dominant scatterers, are depicted in Fig. 5(a)–(c), whereas the respective optical images are shown in Fig. 5(d)–(f). The retrieved parameters are summarized in Table III: the mean value of the percent error is 2.37% and 2.02% for the radial velocity and acceleration, respectively, and 4.27% for the target dimensions.
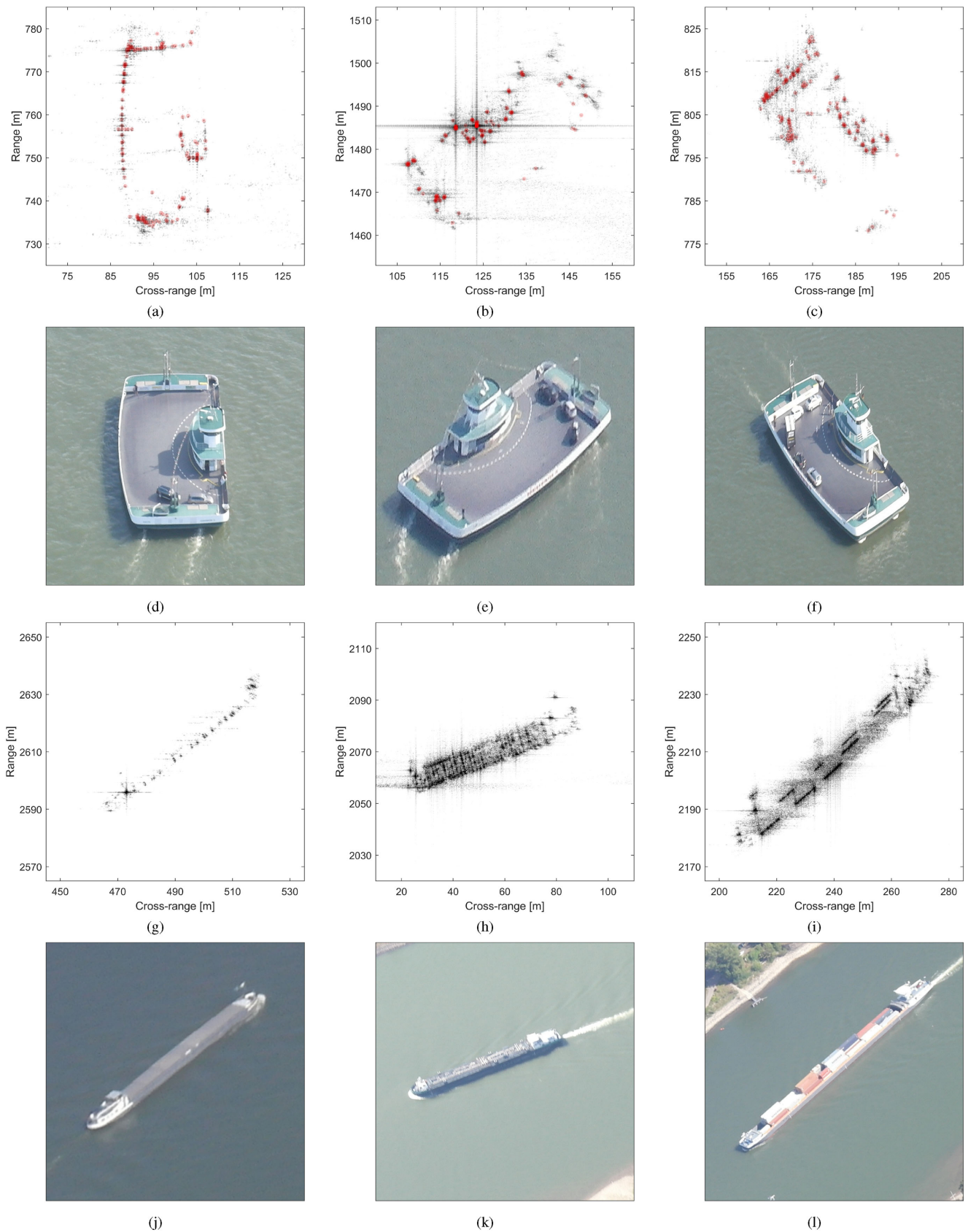
Fig. 5. Experiment 1, data-take #1–3. (a)–(c) Target of interest; range/cross-range images after refocusing and CLEAN images (red). (d)–(f) Target of interest; optical images. (g)–(i) Targets of opportunity; range/cross-range images after refocusing. (j)–(l) Targets of opportunity; optical images.
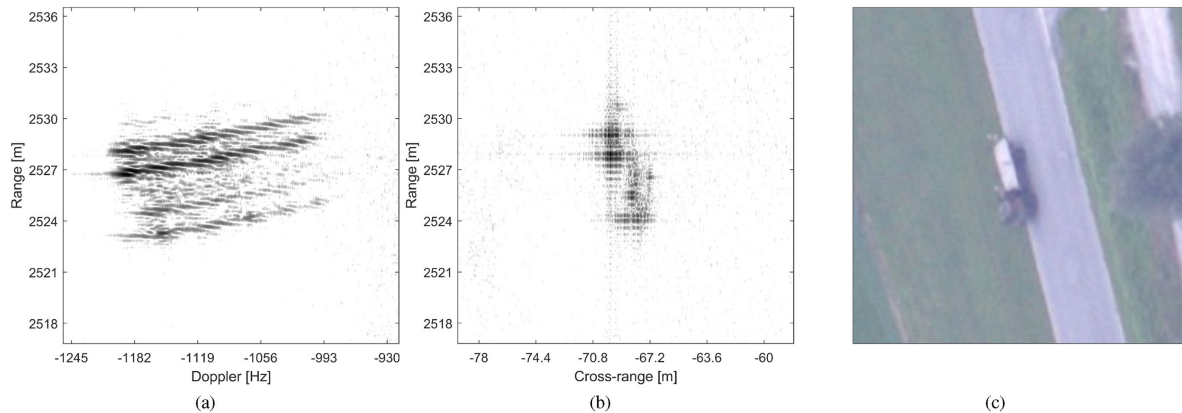
Fig. 6.   Experiment 2, data-take 1. (a) Range/Doppler image before refocusing. (b) Range/cross-range image after refocusing. (c) Optical image.

TABLE IV
RESULTS: EXPERIMENT 2

Data-take	#1	#2	#3
(v_r, ϵ_{v_r})	$(-2.64, 1.18)$	$(-1.89, 2.98)$	$(-1.57, 1.02)$
(a_r, ϵ_{a_r})	$(1.23, 3.23)$	$(0.66, 2.20)$	$(1.00, 1.13)$

*$[v_r] = \text{m} \cdot \text{s}^{-1}$, $[a_r] = \text{m} \cdot \text{s}^{-2}$, $[\epsilon] = \%$.

Additionally, targets of opportunity, for which no direct ground-truth measurements are available (neither motion parameters nor dimensions), were processed: the obtained refocused images are depicted in Fig. 5(g)–(i), and the respective optical images are shown in Fig. 5(j)–(l).

B. Experiment 2

The range/Doppler images before and after refocusing for an exemplary data-take are shown in Fig. 6(a) and (b), respectively, whereas the corresponding optical image is shown in Fig. 6(c). The best degree of focusing is obtained when using $(v_r, a_r) = (-2.64 \, \text{m} \cdot \text{s}^{-1}, 1.23 \, \text{m} \cdot \text{s}^{-2})$, thus defining a percent error of $(1.18\%, 3.23\%)$. The same procedure was then adopted to process the remaining data-takes, thus retrieving the estimates summarized in Table IV: the mean value of the percent error results to be 1.73% and 2.19% for, respectively, the radial velocity and acceleration. As the data-takes were acquired under almost identical configurations, no substantial visual differences arise; thereby, the refocused images of the remaining data-takes are not shown herein.

IV. DISCUSSION

A. Refocusing Algorithm

The performances obtained for Experiment 1 are summarized as follows. The percent error of the radial velocity ranges between 1.78% and 2.67% and has a mean value of 2.37%. As for the radial acceleration, its estimates yielded an error ranging between 0.28% and 5.05%, with a mean value of 2.02%. The resulting refocused images [see Fig. 5(a)–(c)] exhibit strong similarities with the corresponding optical images [see Fig. 5(d)–(f)]. Nonetheless, some structures that are clearly visible for one data-take [e.g., see the left contour of the ferry deck in Fig. 5(a)]

are either barely detectable or even missing in the remaining ones. When interpreting and comparing the visual outputs of Fig. 5(a)–(c), it is worth bearing in mind that they were obtained under different conditions: not only crucial radar parameters such as PRF and bandwidth vary (see Table I), but, more importantly, different illumination conditions (e.g., incidence angle, integration time, etc.) were experienced. A meaningful example is given by the signatures of the parked vehicles on the ferry deck, which clearly emerge from the white (low energy) floor only for data-take #3 [see Fig. 5(c)]. The causes behind such behaviors are not easily traceable, and the explanations proposed herein are merely speculative. One plausible cause is given by the different acquisition geometries: for data-takes #1 and #2, planar surfaces, such as the roof or the vehicles sides, reflect the electromagnetic energy away from the sensor, whereas only edges backscatter a detectable signal.

All targets' signatures were mapped from the range/Doppler domain to the range/cross-range domain after estimation of Ω_{eff}. However, the accuracy of such estimates, and thereby of the resulting dimensions, could be assessed only for the target of interest of Experiment 1. The percent error of the length (i.e., the dimension along the longer main axis) ranges between 3.65% and 6.94% and has a mean value of 4.76%. As for the width (i.e., the dimension of the ferry along its shorter main axis), its estimates yielded a percent error ranging between 3.14% and 4.53%, with a mean value of 3.77%. For all available data-takes, both dimensions were always underestimated. The aforementioned values were obtained by exploiting the CLEAN images: the retrieved dominant scatterers were projected onto the axis of interest, and the pair defining the largest distance was used in order to define the estimate. When adopting such an approach, measurements from different data-takes are not completely coherent with each other as different pairs of dominant scatterers are used to estimate the same geometric feature. Nonetheless, though the images were acquired under completely different conditions, the estimates summarized in Table III are similar; thereby, they represent a reliable indicator of the algorithm performances.

The radar and optical images of three additional targets are shown in Fig. 5(g)–(l), respectively. The amount of backscattered energy is directly linked to the target characteristics: the deck surface depicted in Fig. 5(j) appears to be flat, and as a

consequence, most of the energy is reflected away from the sensor, thus producing an image with only few visible features [see Fig. 5(g)]. On the other hand, Fig. 5(k)–(l) presents surfaces with complicated and edgy structures, thereby justifying the considerable amount of backscattered energy [see Fig. 5(h)–(i)].

Similar to Experiment 1, the GPS-derived values were used to validate the estimates of Experiment 2. The percent error of the radial velocity ranges between 1.02% and 2.98% and has a mean value of 1.73%. The estimates of the radial acceleration, *vice versa*, defined a percent error ranging between 1.13% and 3.23%, with a mean value of 2.19%. Neither the front nor the rear of the truck is clearly imaged in Fig. 6(b), thereby making the image interpretation more difficult. Nonetheless, the following remarks have to be taken into account. The largest ratio of backscattered energy is due to the deployed corner reflectors. However, from a visual inspection of the resulting images, only the pair of reflectors installed in the vehicle's rear is clearly recognizable [see farther contributions in either Fig. 6(a) or (b)]. Identifying the causes that lie behind such behaviors is a challenging task, and validating the findings is no longer possible. A likely explanation is given by an erroneous implementation of the experiment's setup: during the SAR acquisition, and thus while the truck was moving, the reflectors might have shaken, thereby inducing centimeter scale range variations, which cannot be accurately described by the adopted range history model.

One limiting factor of the implemented algorithm is represented by the inability to handle low signal-to-noise-and-clutter ratio environments. The superimposition of clutter, in combination with the spreading of the target energy outside of the cropped subimage, decreases the SCNR and affects the derived estimates. Nevertheless, such effects were minimized due to the adopted experiments' setups. In fact, all targets of Experiment 1 were imaged inside the Rhine river, which backscatters a marginal amount of energy. On the other hand, for Experiment 2, ground-clutter competes with the signal of interest, though the use of corner reflectors makes the useful signal emerge from the stationary background. In light of the above, it is safe to assume clutter to have a limited impact for the cases discussed herein, thus making unnecessary the use of clutter rejecting techniques. However, it remains an open question as to how the performance would degrade in case the aforementioned conditions were not experienced. Moreover, it should be noted that the range registration coordinate for moving targets in FMCW SAR datasets is a function of both round-trip delay *and* Doppler frequency. This, in turn, translates into an invalid range measurement, thereby affecting the estimates of the motion parameters obtained from the range-compressed signal. However, for the examples shown herein, the undesired contribution affecting the radial velocity estimates in Tables III and IV reaches values up to $2 \text{ cm} \cdot \text{s}^{-1}$, and it is, therefore, considered negligible. Finally, it is worth highlighting that the implemented method is designed on the assumption of using short integration times (i.e., of the order of 1s). Within such a time span, the effective rotation vector is approximately constant and the range–Doppler technique is successful. However, when longer integration times are needed to maximize the azimuth resolution, or when the target undergoes exceptionally strong angular motions, the adopted imaging method is no longer optimum, and other solutions are necessary [27].

B. Summary and Outlook

This article has proven the capabilities of FMCW Ka-band datasets for radar imaging purposes. The authors combined a number of state-of-the-art techniques to produce high-resolution images of moving targets. The main core of the implemented algorithm is represented by the range–Doppler technique, which, in combination with autofocusing, allows us to produce radar images with high resolution. Though the deployed method consists of well-known techniques, the authors believe that the results shown herein are of particular importance. First, although the demand for low-cost and compact imaging systems has increased over the past few years, only few publications have dealt with the imaging of moving targets in FMCW SAR environments. Moreover, Ka-band datasets have rarely been used for moving targets imaging, and the resulting products (e.g., images, derived motion parameters and geometric features) have never been validated as thoroughly as in the current work. The choice of the band is crucial in determining the system performances: for a given variation of the viewing angle, shorter wavelengths—or, equivalently, higher frequencies—allows us to obtain a better cross-range resolution. Finally, assessing whether ultra-light-weight airborne platforms are capable of guaranteeing satisfying performances is a question that needs to be addressed as the current technological advances push for the exploitation of even lighter platforms. However, such carriers usually present an unstable motion: for the data-takes discussed herein, the standard deviations of the angular motions result to be at least an order of magnitude larger than that for heavier carriers (e.g., the Transall C-160).

The implemented method has been tested, and its performances have been precisely assessed: the motion estimates were validated by making use of ground measurements, whereas the retrieved target dimensions were compared with the design values obtained from the target construction project. Both motion and geometric estimates resulted to produce marginal percent errors, thereby validating the implemented algorithm and verifying the usefulness of the datasets.

Future research shall focus on designing imaging algorithms, which can successfully process millimeter-wave datasets acquired by SAR sensors mounted on board ultra-light-weight, or even lighter, airborne platforms. As MoComp plays a crucial role in defining the final degree of focusing, especially when exploiting shorter wavelengths, particular attention shall be paid to designing algorithms that are not constrained to simplified range history models. Moreover, choosing whether to use time- or frequency-domain processors is not trivial, as the latter appear to be not sufficiently flexible to handle strongly nonlinear flightpaths. The use of a lighter platform, and thereby of a more compact system, might dictate physical design constraints that prevent from exploiting multiple channels, thus making it impossible to implement efficient clutter rejecting techniques. In light of the above, it is of interest to quantify the minimum SCNR that still allows for an acceptable degree of focusing, and how

the accuracy of the derived estimates degrades as a function of the SCNR. Moreover, particular attention shall be paid to assess how the target angular motions affect the final products, and to modify the implemented method for it to be capable of handling longer integration times. Alternatively, it is also of interest to study the feasibility of merging either coherently or incoherently a sequence of ISAR images after mapping them into a common reference frame.

ACKNOWLEDGMENT

REFERENCES

[1] J. C. Curlander and R. N. McDonough, *Synthetic Aperture Radar*. New York, NY, USA: Wiley, 1991.

[2] S. Brusch, S. Lehner, T. Fritz, M. Soccorsi, A. Soloviev, and B. van Schie, "Ship surveillance with TerraSAR-X," *IEEE Trans. Geosci. Remote Sens.*, vol. 49, no. 3, pp. 1092–1103, Mar. 2011.

[3] A. R. Brenner and J. H. Ender, "Demonstration of advanced reconnaissance techniques with the airborne SAR/GMTI sensor PAMIR," *Proc. Inst. Elect. Eng.—Radar, Sonar Navigat.*, vol. 153, no. 2, pp. 152–162, Apr. 2006.

[4] W. C. Carrara, R. S. Goodman, and R. M. Majewski, *Spotlight Synthetic Aperture Radar: Signal Processing Algorithms*. Boston, MA, USA: Artech House, 1995.

[5] A. Meta, P. Hoogeboom, and L. P. Ligthart, "Signal processing for FMCW SAR," *IEEE Trans. Geosci. Remote Sens.*, vol. 45, no. 11, pp. 3519–3532, Nov. 2007.

[6] R. Perry, R. Dipietro, and R. Fante, "SAR imaging of moving targets," *IEEE Trans. Aerosp. Electron. Syst.*, vol. 35, no. 1, pp. 188–200, Jan. 1999.

[7] J. K. Jao, "Theory of synthetic aperture radar imaging of a moving target," *IEEE Trans. Geosci. Remote Sens.*, vol. 39, no. 9, pp. 1984–1992, Sep. 2001.

[8] S. Zhu, G. Liao, Y. Qu, Z. Zhou, and X. Liu, "Ground moving targets imaging algorithm for synthetic aperture radar," *IEEE Trans. Geosci. Remote Sens.*, vol. 49, no. 1, pp. 462–477, Jan. 2011.

[9] D. Cristallini, D. Pastina, F. Colone, and P. Lombardo, "Efficient detection and imaging of moving targets in SAR images based on chirp scaling," *IEEE Trans. Geosci. Remote Sens.*, vol. 51, no. 4, pp. 2403–2416, Apr. 2013.

[10] V. T. Vu, M. I. Pettersson, and T. K. Sjögren, "Moving target focusing in SAR image with known normalized relative speed," *IEEE Trans. Aerosp. Electron. Syst*, vol. 53, no. 2, pp. 854–861, Apr. 2017.

[11] E. Casalini, M. Frioud, D. Small, and D. Henke, "Refocusing FMCW SAR moving target data in the wavenumber domain," *IEEE Trans. Geosci. Remote Sens.*, vol. 57, no. 6, pp. 3436–3449, Jun. 2019.

[12] J. L. Walker, "Range-Doppler imaging of rotating objects," *IEEE Trans. Aerosp. Electron. Syst*, vol. AES-16, no. 1, pp. 23–52, Jan. 1980.

[13] D. A. Ausherman, A. Kozma, J. L. Walker, H. M. Jones, and E. C. Poggio, "Developments in radar imaging," *IEEE Trans. Aerosp. Electron. Syst*, vol. AES-20, no. 4, pp. 363–400, Jul. 1984.

[14] E. Giusti and M. Martorella, "Range Doppler and image autofocusing for FMCW inverse synthetic aperture radar," *IEEE Trans. Aerosp. Electron. Syst*, vol. 47, no. 4, pp. 2807–2823, Oct. 2011.

[15] S. Stanko *et al.*, "SAR with MIRANDA-millimeterwave radar using analog and new digital approach," in *Proc. 8th Eur. Radar Conf.*, 2011, pp. 214–217.

[16] M. Martorella, D. Pastina, F. Berizzi, and P. Lombardo, "Spaceborne radar imaging of maritime moving targets with the cosmo-skymed SAR system," *IEEE J. Sel. Top. Appl. Earth Observ. Remote Sens.*, vol. 7, no. 7, pp. 2797–2810, Jul. 2014.

[17] R. Wang, O. Loffeld, H. Nies, S. Knedlik, M. Hagelen, and H. Essen, "Focus FMCW SAR data using the wavenumber domain algorithm," *IEEE Trans. Geosci. Remote Sens.*, vol. 48, no. 4, pp. 2109–2118, Apr. 2010.

[18] E. Chapin and C. W. Chen, "Airborne along-track interferometry for GMTI," *IEEE Aerosp. Electron. Syst. Mag.*, vol. 24, no. 5, pp. 13–18, May 2009.

[19] S. Chiu, "A constant false alarm rate (CFAR) detector for RADARSAT-2 along-track interferometry," *Can. J. Remote Sens.*, vol. 31, no. 1, pp. 73–84, 2005.

[20] K. Robinson and P. F. Whelan, "Efficient morphological reconstruction: A downhill filter," *Pattern Recognit. Lett.*, vol. 25, no. 15, pp. 1759–1767, 2004.

[21] R. Klette and A. Rosenfeld, *Digital Geometry: Geometric Methods for Digital Picture Analysis*. San Mateo, CA, USA: Morgan Kaufmann, 2004.

[22] M. Martorella and F. Berizzi, "Time windowing for highly focused ISAR image reconstruction," *IEEE Trans. Aerosp. Electron. Syst*, vol. 41, no. 3, pp. 992–1007, Jul. 2005.

[23] F. Berizzi, M. Martorella, B. Haywood, E. D. Mese, and S. Bruscoli, "A survey on ISAR autofocusing techniques," in *Proc. IEEE Int. Conf. Image Process.*, 2004, pp. 9–12.

[24] F. Berizzi and G. Corsini, "Autofocusing of inverse synthetic aperture radar images using contrast optimization," *IEEE Trans. Aerosp. Electron. Syst.*, vol. 32, no. 3, pp. 1185–1191, Jul. 1996.

[25] M. Martorella, "Novel approach for ISAR image cross-range scaling," *IEEE Trans. Aerosp. Electron. Syst.*, vol. 44, no. 1, pp. 281–294, Jan. 2008.

[26] M. Martorella, N. Acito, and F. Berizzi, "Statistical CLEAN technique for ISAR imaging," *IEEE Trans. Geosci. Remote Sens.*, vol. 45, no. 11, pp. 3552–3560, Nov. 2007.

[27] F. Berizzi, E. D. Mese, M. Diani, and M. Martorella, "High-resolution ISAR imaging of maneuvering targets by means of the range instantaneous Doppler technique: Modeling and performance analysis," *IEEE Trans. Image Process.*, vol. 10, no. 12, pp. 1880–1890, Dec. 2001.

Emiliano Casalini (Member, IEEE) was born in Carrara, Italy, on December 13, 1988. He received the bachelor's and master's degrees (*cum laude*) in telecommunications engineering from the University of Pisa, Pisa, Italy, in 2011 and 2014, respectively. He is currently working toward the Ph.D. degree with the University of Zürich, Zürich, Switzerland.

His research interests include indicating and imaging ground moving targets in synthetic aperture radar (SAR) images, SAR focusing, inverse SAR, interferometry, and other SAR-related techniques.

Julian Fagir (Member, IEEE) received the bachelor's and master's degrees in mathematics from the Technical University of Berlin, Berlin, Germany, in 2013 and 2015, respectively. He is currently working toward the Ph.D. degree with the University of Zürich, Zürich, Switzerland.

His research interests include synthetic aperture radar (SAR)-RGB data fusion, change detection with an emphasis on heterogeneous SAR-RGB change detection, and other remote sensing data-fusion-related techniques.

Daniel Henke received the Dipl.-Inf. degree in computer science from Albert-Ludwigs University, Freiburg, Germany, in 2007, and the Ph.D. degree from the University of Zürich, Zürich, Switzerland, in 2014.

His Ph.D. dissertation focused on the development of methods to track objects in remotely sensed data. From 2014 to 2017, he was a Postdoctoral Researcher under a University Research Grant with the SARLab, University of Zürich, and under the SNF Postdoctoral Mobility Grant with the Department of Earth System Science, School of Physics, University of California, Irvine, CA, USA, and the Smithsonian Tropical Research Institute, Panama, Panama. Since 2017, he has been leading the Computational SAR Group, SARLab, Remote Sensing Laboratories, University of Zürich. His research interests include synthetic aperture radar processing, moving target indication and change detection techniques, data fusion, signal processing, probabilistic modeling, and Earth system science applications using remote sensing data.